A GCN-Based Method for Extracting Power Lines and Pylons From Airborne LiDAR Data

Wen Li, *Student Member, IEEE*, Zhipeng Luo, *Student Member, IEEE*, Zhenlong Xiao, *Member, IEEE*, Yiping Chen, *Senior Member, IEEE*, Cheng Wang, *Senior Member, IEEE*, and Jonathan Li, *Senior Member, IEEE*

***Abstract*— Extracting the power lines and pylons automatically and accurately from airborne LiDAR data is a critical step in inspecting the routine power line, especially in the remote mountainous areas. However, challenges arise in using existing methods to extract the targets from large scenarios of remote mountainous areas since the terrain is undulating, and the features are difficult to distinguish. In this article, to overcome these challenges, we propose a graph convolutional network (GCN)-based method to extract power lines and pylons from Airborne LiDAR point clouds. First, data augmentation and near-ground filtering methods are developed to overcome the problems of insufficient and imbalanced samples in the LiDAR data. Then, a GCN-based framework is proposed to extract the power lines and pylons, which consist of two main modules, i.e., the neighborhood dimension information (NDI) module and the neighborhood geometry information aggregation (NGIA) module. These two modules are designed to strengthen the model's ability to portray local geometric details. Besides, an attention fusion module is investigated to further improve the NDI and NGIA features. Finally, a line structure constraint algorithm is proposed to identify individual power lines, where the power corridor is reconstructed using a polynomial-based algorithm. Numerical experiments are conducted based on two different power line scenarios acquired in mountainous areas. The results demonstrate the superior performances of the proposed method over several existing algorithms, where the F_1 score and quality of the power line are 99.3% and 98.6%, and the results of the pylon are 96% and 92.4%, respectively. The identification rate of power line identification is above 98%.**

***Index Terms*— Airborne LiDAR, graph convolutional network (GCN), neighborhood information, power line extraction, pylon extraction.**

Manuscript received October 31, 2020; revised March 4, 2021; accepted April 3, 2021. This work was supported in part by the National Natural Science Foundation of China under Grant 61801410 and Grant 41871380; in part by the Natural Science Foundation of Fujian Province of China under Grant 2019J01004; and in part by the Natural Sciences and Engineering Research Council of Canada under Grant 50503-10284. *(Wen Li and Zhipeng Luo contributed equally to this work.) (Corresponding authors: Zhenlong Xiao; Jonathan Li.)*

Wen Li, Zhipeng Luo, Zhenlong Xiao, Yiping Chen, and Cheng Wang are with the Fujian Key Laboratory of Sensing and Computing for Smart Cities, School of Informatics, Xiamen University, Xiamen 361005, China (e-mail: zlxiao@xmu.edu.cn).

Jonathan Li is with the Department of Geography and Environmental Management and the Department of Systems Design Engineering, University of Waterloo, Waterloo, ON N2L 3G1, Canada (e-mail: junli@uwaterloo.ca).

Digital Object Identifier 10.1109/TGRS.2021.3076107

I. Introduction

ELECTRICITY plays an indispensable role in social production, and a large number of transmission lines have been built to meet the civil and industrial needs [1]. Since power grids are interconnected, blackouts in a local region can trigger a cascade reaction, leading to super-regional blackouts [2]. To ensure the reliable transmission of electricity, periodical power line patrol should be arranged since power lines are susceptible to vegetation erosion and natural disasters, which would be a challenge, especially in remote mountainous areas.

The traditional power line extraction methods are labor-intensive, time-consuming, and expensive [3]. With sensor technology development, more and more remote sensing data are used to improve extraction performance. They can be divided into two categories: the image-based data such as synthetic aperture radar (SAR) images [4] and aerial images [5], and 3-D point-based data such as airborne laser scanning (ALS) or airborne LiDAR data [6] and mobile laser scanning (MLS) data [7]. Several image-based methods have highly impressive results, which would still suffer from disturbances such as occlusion, self-occlusion, and light changes [8]. ALS can obtain 3-D shape information of the power line accurately and efficiently over a large area, especially in the difficult-to-reach mountainous areas. Therefore, ALS point clouds would be more suitable for the extraction of power lines and pylons. In this article, we focus on the extraction of power lines and pylons from ALS point clouds.

Power line and pylon extraction methods using point clouds can be divided into three stages: data preprocessing, power line and pylon segmentation, and refinement [9]. The preprocessing step aims at removing the outliers and part of the ground points away from the scene. Note that the power lines are usually located far above the ground for safety reasons, ground filtering, such as triangular irregular network densification filtering [10] and cloth simulation filtering [11] have been undertaken to identify and separate the ground points. However, these methods would lose part of the pylon points because the surface of mountainous areas is undulating.

Power line and pylon segmentation is the most important stage in the extraction process. In this phase, the objects in the scene are classified as power lines, pylons, and others.

Existing point clouds segmentation methods can be divided into two categories: traditional descriptor-based methods and deep learning (DL)-based methods. The traditional descriptor-based methods aim at designing the local geometric features by handcrafting to obtain segmentation results. These methods can be further subdivided into unsupervised [12]–[15] and supervised [16]–[19] methods. A multiheight threshold method was proposed [13] for separating power lines and pylon points in multiple subspaces of the original point clouds. In [14], principal component analysis (PCA) was utilized to extract power lines and pylons. In [16], some features, e.g., height, were designed to describe power lines and pylons, and the segmentation results were then obtained by feeding it to the random forests method. To improve the robustness, in [18], a multiscale oblique cylindrical neighborhood-based method was developed to extract spatial structural features. Several image processing methods can be used after transforming the point clouds into regular data representations, such as 3-D voxel [20]–[22] and 2-D images [23], [24]. Similarity detection and random sample consensus (RANSAC) methods were combined in [20] to detect the data distribution characteristics and estimate the power line model. Hough transform (HT) and compass line filter [23] were applied to determine the transmission line area and direction, and combined F distribution to extract power line points. However, these methods usually require additional supporting information, such as intensity, preclassified data, or return numbers. Moreover, the parameter setting for these methods would be complicated with different point clouds distribution in different scenarios. Even worse, these methods cannot learn the complete structure information for pylons.

The above segmentation methods may achieve satisfactory results in simple scenes. However, features learned by these methods are usually shallow and difficult to distinguish, which would be unfavorable in complex scenes, such as remote mountainous areas. In recent years, DL [25] has demonstrated good performance in feature extraction [26], classification [27], and segmentation [28]. On 3-D point clouds processing, DL-based methods can be divided into four categories: view-based [29], [30], voxel-based [31], [32], point-based [33], [34], and graph-based [35], [36]. PointNet [33] was the first one to process point clouds directly, which process each point independently and merges per-point features into a global feature by the max-pooling operation. In this way, local features between neighborhood points may lose. Therefore, several improved methods are proposed, such as PointNet++ [37] and PointConv [38]. However, these methods do not fully exploit the information among different points. To obtain local features, graph-based methods take the k nearest neighbor points into consideration when calculating the features of each point. DGCNN [35] constructed local graphs to represent local information, and updated the graph in the feature space to extract features hierarchically. These methods can achieve promising results in some indoor [39], [40] and outdoor [41], [42] datasets, where a large amount of labeled data are required. As far as we know, there is no result in the literature using DL to segment power lines and pylons using 3-D point clouds, which would be caused by the following two reasons: insufficient data and unbalanced samples in the scenarios. These motivate us to propose a data augmentation method and a near-ground filtering method to solve these two challenges.

The refinement phase consists of two steps, i.e., the individual power line identification and reconstruction. First, each power line is further identified from the classified power line points, for example, using the clustering and fitting polynomial-based methods or detection-based methods. RANSAC [14], [20] is applied to determine the points belonging to the same line according to the distance constraints. The alignment characteristics of the wires [22] in voxelized point clouds are utilized to extract a single wire point. The fitted polynomials are used for the power line reconstruction [43].

There are still several challenges in extracting power lines and pylons using point clouds. One of the problems is the immense data volume of point clouds, which leads to the computational bottleneck of the target extraction. Note that several objects, such as ground and vegetation points, are much denser than power lines and pylons points. Reliable extraction of points of interest with imbalanced samples would be the second challenge. Existing methods may achieve good results. However, these tend to use several additional supplemental data types, for example, the intensity, preclassified data, and return numbers. Moreover, the extracted object structures of interest are usually incomplete as the adopted features are not easy to distinguish, time-consuming and complicated in parameter settings.

In this article, we aim at investigating a new method for extracting power lines and pylons from ALS point clouds using only the xyz coordinate information. Our main contributions are as follows.

1) In theory, we explore the graph convolution on point cloud feature extraction and propose two modules, neighborhood dimension information (NDI) and neighborhood geometry information aggregation (NGIA), to study the effect of point neighborhood information on point cloud representation learning. Numerical experiments show that these modules can strengthen the ability of the proposed method to characterize the details and to extract objects completely. This indicates that the neighborhood information is helpful to improve the point cloud feature extraction. Besides, we propose an effective method for data augmentation and near-ground filtering to mitigate the challenges of insufficient data and imbalanced samples, which is of great help to the training of our method.
2) In practice, we propose a framework based on graph convolution, which can extract power lines and pylons efficiently and accurately. Specifically, our method extracts the target with more complete structural information and takes less time than traditional methods. Compared with DL-based methods, the extracted targets by our method contain more detailed information. Moreover, our method is more robust to occlusion and can be applied to several complex scenes. The experimental results demonstrate the superior performances of the proposed method, where the F_1 score and quality of the power line are 99.3% and 98.6%, and the results

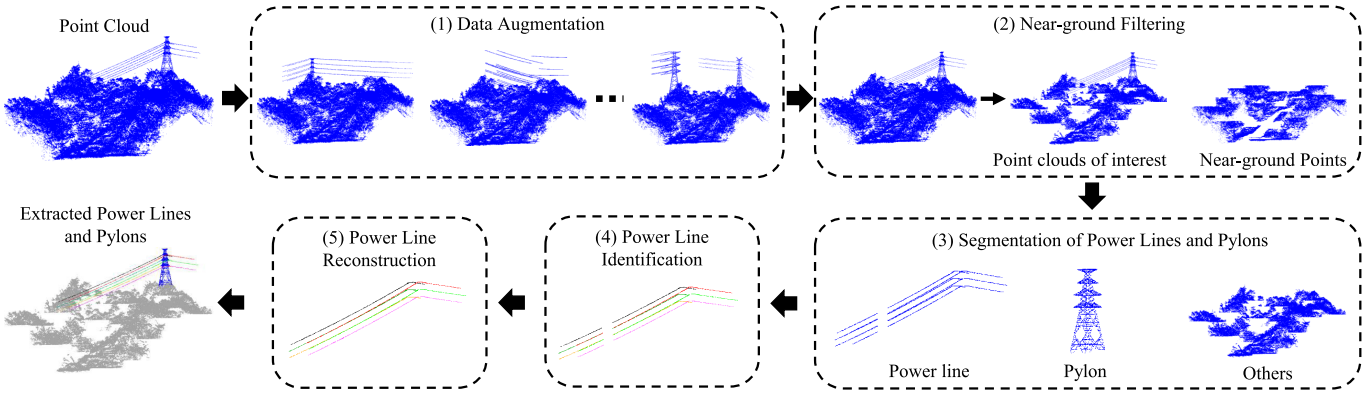

Fig. 1. Key steps of our proposed methods. The first and second steps are preprocessing stages, while the last three steps are the main parts.

of the pylon are 96% and 92.4%, respectively. The identification rate of power line identification is above 98%.

The rest of this article is organized as follows. Section II presents the proposed GCN-based method, and Section III conducts the numerical experiment. Section IV shows the key points and limitations of the proposed method, and Section V concludes this article.

II. Proposed Method

In this section, we present the proposed method to extract the power lines and the supporting pylons. Our input is the unorganized point clouds involving only *xyz* coordinate information obtained by ALS, and we do not require any supplemental information, such as reflection intensity or pre-classified data. The outputs are the individually segmented power lines and pylons. Our proposed method consists of four main steps: 1) data augmentation to provide sufficient training data; 2) near-ground filtering to remove outlier points within a certain height from the ground; 3) GCN-based method to segment the power line and pylon points; and 4) power line identification and reconstruction to identify individual power lines and recover broken sections, respectively. The key steps of the proposed method are shown in Fig. 1.

A. Data Augmentation and Near-Ground Filtering

Data Augmentation: Generally, with more training data, more descriptive features of the model can be learned from the point clouds [44]. Therefore, a feasible data augmentation strategy must be designed first. Two possible methods are rotation and sample overlap for power line scenarios, but these two augmentation methods will cause limited data diversity and volume.

To solve the above issues, we design a feasible data augmentation method, as shown in Fig. 2. This method consists of three main steps: 1) segmenting the training data into several segments with given predesigned sizes; 2) dividing each segment into three categories: ground (including vegetation), pylon, and power line; and 3) selecting randomly from each category and combining them to obtain new samples.

Near-Ground Filtering: Sample imbalance is unavoidable in the power line scenario. The ground (including vegetation)

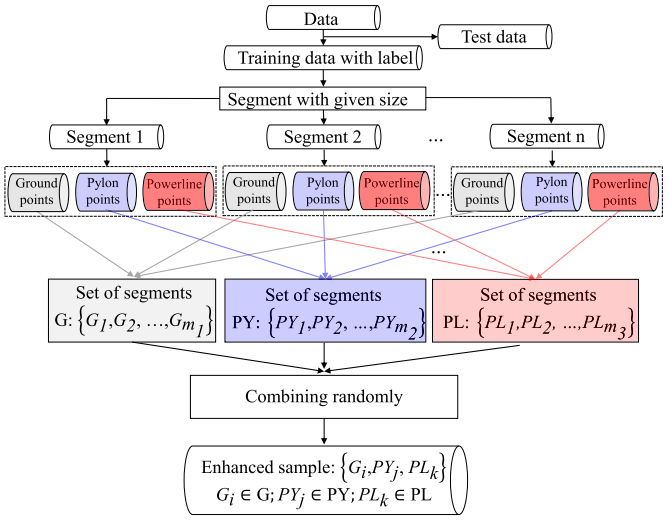

Fig. 2. Flowchart of our data augmentation approach.

points usually account for more than 90% of the total points. Using unbalanced data to train the model will lead to an unsatisfactory result [16]. In the transmission line scene, the ground points are dense and the power line points are usually distributed with a relative height. Therefore, we propose a multithreshold near-ground (MTNG) filtering method to reduce ground points as much as possible while maintaining power line and pylon points, which contains the following steps: 1) dividing the original scene into multiple small scenes with a length and width of 20 m, and ranking all points from the highest to the lowest z; 2) checking whether there are power line points according to the difference between the maximum and average value in the small scene; and 3) using a multithreshold strategy to extract n_{new} points in the small scene:

$$n_{\text{new}} = \begin{cases} 15000, & \text{if } (\max(z)\text{-mean}(z)) \geq 10 \& n \geq 15\,000 \\ n, & \text{if } (\max(z)\text{-mean}(z)) \geq 10 \& n < 15\,000 \\ 10000, & \text{if } (\max(z)\text{-mean}(z)) < 10 \& n \geq 10\,000 \\ n, & \text{if } (\max(z)\text{-mean}(z)) < 10 \& n < 10\,000 \end{cases} \quad (1)$$

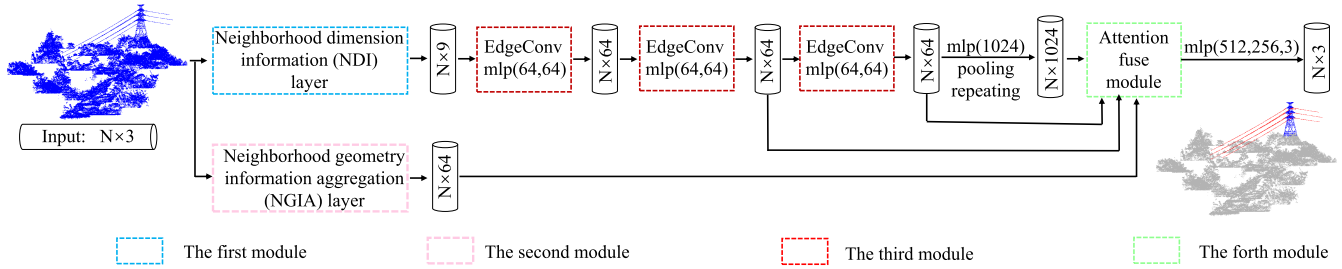

Fig. 3. Flowchart of the proposed GCN method. NDI module provides local information to improve the ability to capture detail spatial structure, while NGIA module is designed to obtain neighborhood geometry information from each point to improve local shape description ability. EdgeConv module obtains neighboring edge features. AF module is utilized to aggregate the features extracted from the upper and lower branches.

where n is the original number of points in each part, max(·) and mean(·) represent the maximum and average values in each part respectively, and n_{new} is the number of points extracted in each part.

B. Power Lines and Pylons Segmentation

GCN models have been proved powerful in mining global shape features. To accurately and efficiently segment power lines and pylon points from the scene, we propose a dual-branch network method, as shown in Fig. 3, which consists of four modules: NDI module, NGIA module, edge convolution (EdgeConv), and attention fusion (AF) module. NDI module is designed to calculate the dimension features of the point clouds, thereby enriching the input information and providing the network with local geometric features of the input point clouds. After multiple convolutions of the input information based on the NDI module, a distinguished global feature can be obtained. However, extraction of local geometric features is still challenging. Therefore, NGIA module is proposed to obtain shallow geometric information and to aggregate information through multilayer perceptron (MLP) and max-pooling layer to enhance the local geometric descriptiveness of the network. EdgeConv module is applied to extract and integrate local information, and the attention fusion module is utilized to aggregate the features extracted from the upper and lower branches. The proposed dual-branch method is described in detail as follows.

1) NDI Module: The original point clouds contain only the *xyz*-coordinate values, which may be insufficient for the extraction of power lines and pylons because it is difficult for the model to distinguish power line features from natural landscapes. Inspired by the studies [14] and [45], we find that in power line scenes, different types of objects vary greatly in shapes. In a certain neighborhood, the power lines, pylons, and ground points are liner, planer, and spherical structure, respectively. Given a point $p \in P$ and a radius ζ, we can obtain a set of neighborhood points $\{p_i || p - p_i| \leq \zeta\}$. Then eigenvalues λ_1, λ_2, and λ_3 ($\lambda_1 \geq \lambda_2 \geq \lambda_3$) can be generated by PCA and the three-dimensional features can be defined as follows:

$$(a_{1D}, a_{2D}, a_{3D}) = \left(\frac{\lambda_1 - \lambda_2}{\lambda_1}, \frac{\lambda_2 - \lambda_3}{\lambda_1}, \frac{\lambda_3}{\lambda_1}\right) \tag{2}$$

where $a_{1D} + a_{2D} + a_{3D} = 1$.

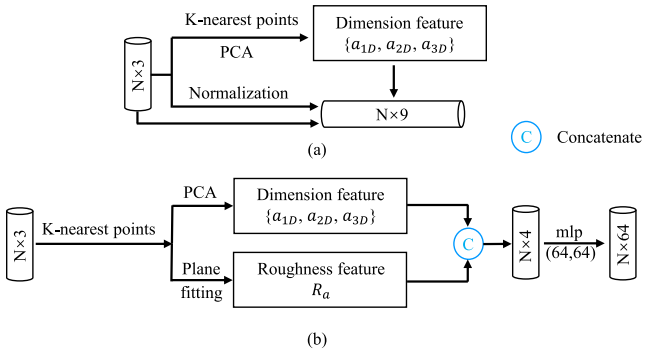

Fig. 4. Structures of (a) NDI and (b) NGIA modules.

In the case of scattered points, such as ground points, we observe that $\lambda_1 \cong \lambda_2 \cong \lambda_3$ and there is no dominant direction. While in the case of a line structure, such as power line points, the principal direction is the tangent at the curve, where $\lambda_1 \gg \lambda_2$ and $\lambda_1 \gg \lambda_3$. Through this local geometric description algorithm, we can increase the prior knowledge of the model, therefore enhancing the model discrimination of objects with different kinds of shapes.

As shown in Fig. 4(a), we use the k-nearest neighbor (k-NN) search algorithm to search for the k neighbors in the neighborhood of the points to calculate the dimension features and normalization, respectively, and then feed them into different channels of the input data. Each point is represented by a 9-D vector, i.e., (xyz, $a_{1D}a_{2D}a_{3D}$, normalized locations).

2) NGIA Module: NDI module can enrich the input information and provide a local feature of the shape, but it is difficult to retain the acquired geometric information after MLP completely. Therefore, we design a short branch, which involves convolution and max-pooling operation to aggregate geometric shallow features to describe local details.

When constructing a directed graph $\mathcal{G}$, it is necessary to search for neighborhood points, which create conditions for us to calculate the geometric features of local point clouds. Meanwhile, the distribution of ground points is disordered and uneven, and the density is relatively high, while the distribution of power lines and pylon points has obvious geometric characteristics. Therefore, we use dimension and roughness features to describe the geometric information of point clouds. The dimension features have been calculated in the NDI module, and we apply them again to reduce the amount of calculation.

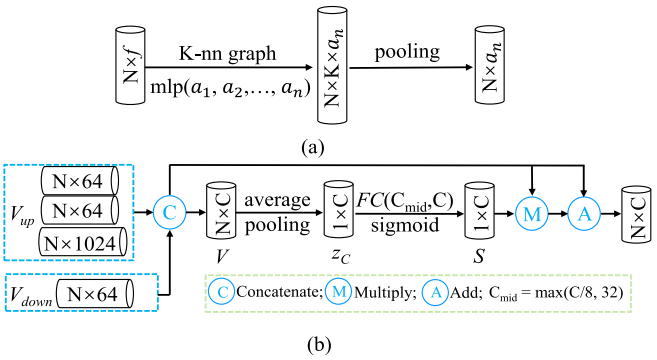

Fig. 5. Structures of (a) EdgeConv and (b) AF modules.

In a certain neighborhood, it is difficult for some points to have obvious geometric structure, especially at the junction of two classes of points, so we add the following roughness feature to enhance the description ability of these points. For the input n points, we calculate the plane $z = ax + by + c$ to make $\sum_{i=1}^{n}(z_i - z)^2 = \sum_{i=1}^{n}(z_i - (ax_i + by_i + c))^2$ and get the minimum value. The roughness feature is then defined as follows:

$$R_a = \frac{\sum_{i=1}^{n}(z_i - z)^2}{K} \tag{3}$$

where z is the plane obtained by the least-squares fitting method, z_i represents the z coordinate of point p_i, and K represents the number of neighboring points.

As shown in the second module in Fig. 4(b), after obtaining the dimension feature and the roughness feature, the 4-dim feature vector $(a_{1D}, a_{2D}, a_{3D}, R_a)$ is extracted for each point. We use MLP and max-pooling aggregate information to obtain feature map V_p, which is computed as

$$V_p = \max(\mathrm{MLP}(a_{1D}, a_{2D}, a_{3D}, R_a)) \tag{4}$$

where V_p denotes the features with shape $N \times 64$ (N points with features of 64 dimensions) and $\max(\cdot)$ represents max-pooling operation.

3) EdgeConv Module: Regular structure, such as image, uses the size of the convolution kernel to define the local region in the image [46]. For the irregular structure of the graph, k nearest to a point is defined as the neighbor of the center points. EdgeConv [35] computes a directed graph $\mathcal{G} = (\mathcal{V}, \mathcal{E})$ to represent the local point clouds structure, where $\mathcal{V} = \{1, \ldots, n\}$ and $\mathcal{E} \subseteq \mathcal{V} \times \mathcal{V}$ are the vertices and edges, respectively. They define the edge feature as $e_{ij} = h_\theta(x_i, x_j - x_i)$, where h_θ is a nonlinear function with a set of learnable parameters θ. As shown in Fig. 5(a), the local feature x'_{im} can be computed as

$$x'_{im} = \max_{j:(i,j)\in\mathcal{E}} \mathrm{ReLU}\left(\theta_m \cdot \left(x_j - x_i\right) + \phi_m \cdot x_i\right) \tag{5}$$

where x'_{im} is a tensor with shape $N \times a_n$ (N points with features of a_n dimensions) and $\theta = (\theta_1, \ldots, \theta_n, \phi_1, \ldots, \phi_n)$ represent the parameters of the neuron in the MLP.

4) AF Module: As shown in Fig. 3, the network can be divided into up and down branches, and each branch obtains different levels of features based on different inputs. Fusing features is the key task in the multimodule methods. Attention mechanism has proved its effectiveness in many fields, such as image classification [47] and object detection [48]. Therefore, we use the attention mechanism proposed in [49] to aggregate the features extracted from the up and down branches.

The output V_{up} and V_{down} of up and down branch are combined by a connection operation to obtain a C-dim feature map V, which is the input of AF module. Then, as shown in Fig. 5(b), an average pooling operation along with the channel are taken on V to generate the global feature z_C, and a soft attention mask S is computed by using a two-layer fully connection (FC) and a sigmoid function as follows:

$$S = \mathrm{sigmoid}(\mathrm{FC}(z_C)) \tag{6}$$

where the attention mask S can be considered as a feature filter to adaptively select meaningful features and restrain the useless ones. To fuse the attention mask more effectively, the residual connection is applied, and the final output can be represented as

$$O_{\mathrm{AF}} = V \times (1 + S) \tag{7}$$

where $\times$ denotes the elementwise multiplication.

After adding AF module, each channel of the feature map obtained by the up and down branches gets the weight. Therefore, the model has a more distinguishing ability for the characteristics of each channel.

C. Power Line Identification and Reconstruction

In this section, candidate power line points need to be further processed to obtain individual wire. Power lines conform to the fact that they do not intersect by each other, and they maintain enough clearance to avoid unsafe contact [50]. Based on these characteristics, we design a line structure constraint (LSC) algorithm, which stably identifies individual power line points and reconstructs the power line by fitting a polynomial equation. The steps are presented as follows.

1) Span Extraction: The transmission wires in a power line corridor are made up of number of segments (spans). Pylons connect these spans to each other. In the previous step, we have extracted the complete pylon points. After determining the position of the pylons by density-base clustering, the points P for each span are obtained. The span extraction reduces the number of data points and makes further processing of line points easier.

2) Power Line Identification: The flowchart of our LSC is shown in Fig. 6. Let $P_r \subset P$ be the set of points that have not been processed, and the initial seed point is selected randomly from P_r. The point $p_s \in P_r$ is selected as a reasonable initial seed point when the distance from p_s to its nearest point is less than d_s given by the user. We denote R_C as the initial point set of an individual power line and add the reasonable seed point and its nearest into R_C.

Next, the criterion that controls the growth from the seed points to their neighborhood points is defined as the point-to-plane distance threshold d_{p_1} and d_{p_2} given by the user. For the neighborhood point $p_i \in P_S^k$, the plane p_1 and vertical plane p_2 are fitted by all the points in R_C, so p_i is added to

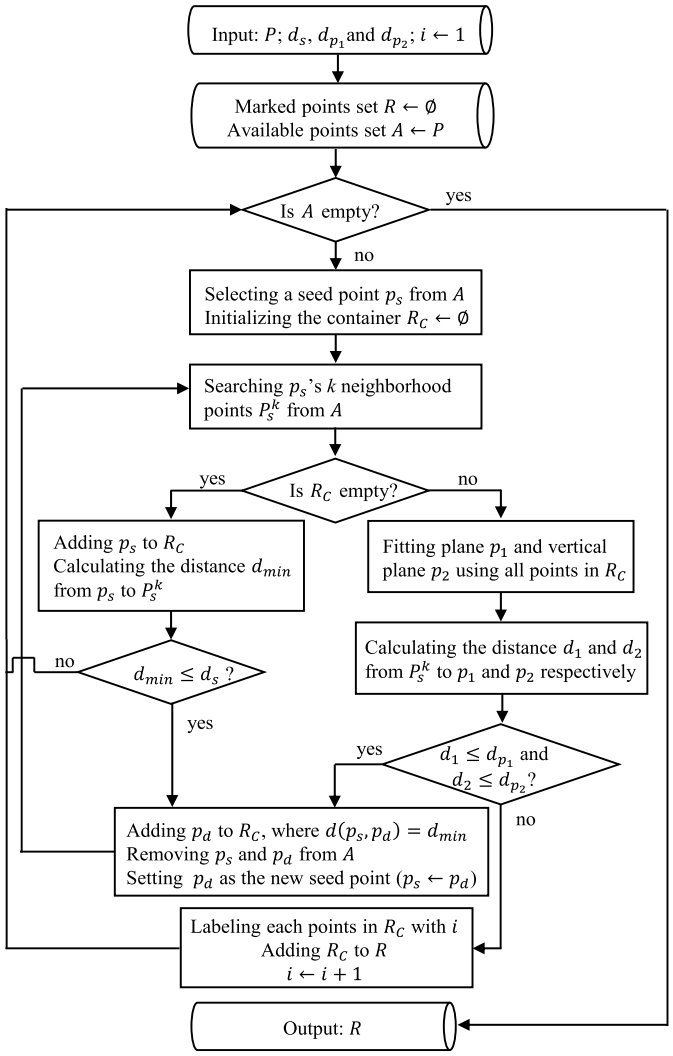

Fig. 6. Flowchart of our LSC approach. P is the power line points of a span. d_s, d_{p_1}, and d_{p_2} are the distance thresholds given by the user.

the R_C if $d_1 < d_{p_1}$ and $d_2 < d_{p_2}$ where d_1 and d_2 represent the distance from to plane p_1 and p_2, respectively. Then, the point $p_i \in R_C$ is removed from P_r.

The newly added point is set as the new seed point. The region growth from the newly selected seed points and the selection of new seed points are performed iteratively until no unique seed point can be chosen. Then, the points in R_C are labeled and added to the output set R. For points in the P_r, iterative processing until all points have been processed.

3) Power Line Reconstruction: After extracting and identifying the point of an individual power line, the final step is to reconstruct these power line points for subsequent applications such as 3-D measurement.

The 3-D power line reconstruction problem is to find the correct model to fit the power line and realize the 3-D visualization. We use polynomial equations (8) in 3-D space to calculate the parameters based on individual power line points, and finally reconstruct the power lines by

$$z = a\left(x^2 + y^2\right) + b\sqrt{x^2 + y^2} + c \tag{8}$$

where a, b, and c represent the parameters to be fitted.

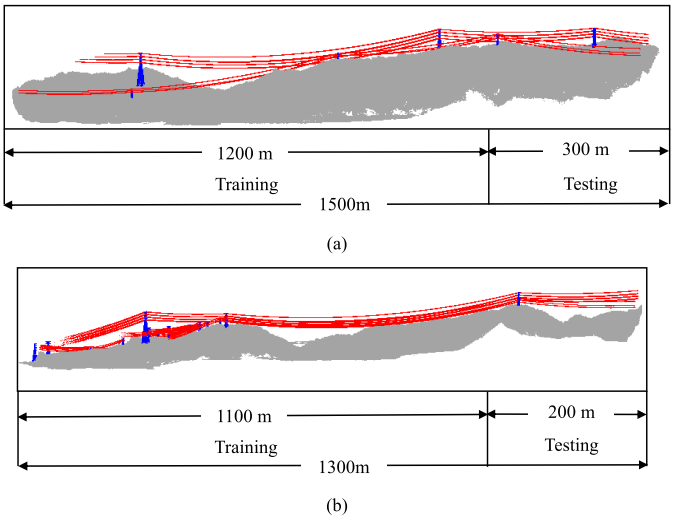

Fig. 7. Overview of datasets. The power line, pylon and ground (including vegetation) are colored in red, blue, and gray respectively. (a) S_I. (b) S_{II}.

TABLE I
STATISTICS OF TEST DATA

Data set		Elevation (m)			Density (points/m^2)
		Highest	Lowest	Average	
S_I	T_1	255.11	153.43	197.07	79
	T_2	261.72	155.51	204.32	78
	T_3	256.28	145.41	204.73	79
Average		257.7	151.45	202.04	78
S_{II}	T_1	242.75	147.83	192.84	91
	T_2	240.32	128.25	179.49	73
Average		241.54	138.04	186.17	82

III. EXPERIMENTS AND ANALYSIS

A. Experimental Data and Environment

To evaluate the effectiveness of our proposed method, we conducted qualitative and quantitative evaluations on two different types of power line scenarios with simple and complex conditions from airborne LiDAR data. The experimental data are collected by HawkScan X3, the flying speed is 24 m/s, the altitude is 150 m, the scanning frequency is 400 kHz, and the point density is about 80 points/m^2. S_I is a simple case, and most areas have a single transmission line corridor. As shown in Fig. 7(a), the length is approximately 1500 m and 300 m of which are chosen as test scenes. As shown in Fig. 7(b), S_{II} is a complex case, with multiple transmission line corridors in most areas. The length is approximately 1300 m, 200 m of which is chosen as the test scene. Table I lists several statistical data of the test scenes, which shows that the ground fluctuates obviously. To better demonstrate our method, we divide the S_I into T_1, T_2 and T_3 and S_{II} into T_1, T_2. These divisions into multiple scenarios here are only for a better display. In practical applications, our method can be applied to scenes of any size.

As shown in Fig. 7, although the data include a wide range of power line corridors, the number of pylons is sparse. For the network, to learn more discriminating features of the pylons, it is necessary to perform data augmentation. The number of original scenarios with pylons is only a dozen, and after

data augmentation, we generate 200 different training scenes per dataset, which significantly increases the training data for learning.

Our experimental platform is Ubuntu 18.04, Inter (R) Xeon(R) E5-2678 v3 2.50 GHz, and 64-GB memory. We trained our method with TensorFlow on NVIDIA GeForce RTX 2080 Ti. Adaptive moment estimation was used with a momentum of 0.9. We set the initial learning rate to 0.001 and decrease by half in every 20 epochs. The batch size is 16, and the number of training epochs is 30. For convenience, we refer to [35] and set the number of neighborhood points to 20. Considering the real situation, we set the parameters d_s, d_{p_1} and d_{p_2} in our LSC method to 0.1, 0.25, and 5 m, respectively. In the power line and pylon points segmentation stage, we use F_1 score (F_1) and quality (Q_u) as the evaluation index

$$F_1 = \frac{2 \times P_{\text{recision}} \times R_{\text{ecall}}}{P_{\text{recision}} + R_{\text{ecall}}} \tag{9}$$

$$Q_u = \frac{TP}{TP + FP + FN} \tag{10}$$

where TP denotes the power lines and pylons that are correctly segmented. FP represents the others that are incorrectly segmented as power lines and pylons. FN denotes the power lines and pylons are incorrectly segmented as others. P_{recision} and R_{ecall} denote precision and recall rate, respectively.

B. Near-Ground Filtering Results

To evaluate the near-ground filtering performance, we used the test scene as an example to compare the changes in the number of points of each category before and after filtering. It can be seen from Table II that after near-ground filtering, the loss of power line and pylon points are no more than 2%, but the ground points (including vegetation) are reduced by nearly two-thirds (more than 400 000 points). In scene S_{II}/T_1, since the ground is undulating and the high vegetation is near the pylon, some points are removed incorrectly. This result can be improved by further reducing the size of the scene. Our approach can be adapted to the slope by dividing the original scene into multiple subscenes and ordering the points within the small scenes. Both the work in [13] and our experimental results demonstrate the feasibility of removing some of the ground points in mountain areas by dividing them into small scenes. In conclusion, there is almost no change in the number of the pylon and power line points, while the ground points are greatly reduced, which proves the effectiveness of this method. All of our next experiments are based on samples after the near-ground filtering.

C. Power Line and Pylon Segmentation Results

To further verify the effectiveness and robustness of our method, we compared our method with several existing segmentation methods. Since we did not find an open-source algorithm, we tried to reproduce two representative methods, which use PCA to calculate dimension features and use small angles between the power line points to segment the power lines and pylon points, called PCA and SAL, respectively. These two methods use CSF filtering [11] to separate ground and non-ground points, and then classify power line and pylon points by setting reasonable thresholds. In addition, we also used the methods in [33] and [38] for comparative experiments.

TABLE II
COMPARISON OF THE NUMBER OF RAW DATA AND FILTERED RESULTS

Data set		Raw point clouds			Filtered results		
		Pylon	Line	Ground	Pylon	Line	Ground
S_I	T_1	-	7,395	792,686	-	7,395	267,605
	T_2	5,600	7,660	783,645	5,600	7,653	261,747
	T_3	-	8,384	793,341	-	8,375	276,625
Average		5,600	7,813	789,891	5,600	7,808	268,659
S_{II}	T_1	8,653	10,673	911,927	8,542	10,670	355,788
	T_2	-	8,090	731,216	-	8,080	366,920
Average		8,653	9,382	821,572	8,542	9,375	361,354

Table III and Fig. 8 show quantitative and qualitative comparison results of different methods, respectively. Compared with the traditional methods PCA and SAL, in the scene where the pylon exists, the F_1 and Q_u of the power line are improved by 31.5% and 45.5%, and that of the pylon increases by nearly 47.1% and 58.8%. In the scene without pylons, the F_1 and Q_u of the power line rise by nearly 2.2% and 3%. It is also obvious from Fig. 8 that there are a large number of misclassified points in the traditional method, and most of these points should be easily distinguished. Our method can well distinguish these points. The reason is that our method can extract more distinctive features than traditional methods. Compared with PointNet, our method also has great advantages. Specifically, PointNet performs poorly in some scenarios, such as S_I/T_2 and S_{II}/T_1, while our method increases F_1 and Q_u of power lines by 19.5% and 31.5%, and that of pylons by 44.6% and 57.8%, respectively. Fig. 8 also shows that our method can extract targets well, and the targets extracted by our method are complete. This is due to the neighborhood points and the local geometric information involved in our method. As shown in Tables III and V, PointConv achieves much better results than DGCNN, but there is still a gap when compared with our method. Specifically, in the scene where the pylon exists using our methods, the F_1 and Q_u of the power line are increased by 2.5% and 4.6%, and that of the pylon are improved by 4.1% and 7.1%. Moreover, our method also has obvious advantages in the scene without pylons. The reason is that our proposed module can learn more detailed features, which is also proved in Fig. 8.

We also compared the time efficiencies of different methods in Table IV. Obviously, DL-based methods take less running time (RT) than the traditional method because the adopted parallel computing, while the traditional methods need to process point-by-point. Compared with DL-based methods, our method takes more RT because of the EdgeConv, NDI, and NGIA in our GCN framework. Such time-consumption is acceptable when considering the much better final extraction results.

D. Effectiveness of Each Proposed Module

To evaluate the effectiveness of our proposed module, we designed a series of ablation experiments. Table V shows the performance changes of the model with the addition of

TABLE III

PERFORMANCE COMPARISONS AMONG DIFFERENT SEGMENTATION METHODS IN F_1 SCORE (%) AND QUALITY (%)

Data set		PCA				SAL				PointNet				PointConv				Ours			
		Pylon		Line		Pylon		Line		Pylon		Line		Pylon		Line		Pylon		Line	
		F_1	Q_u	F_1	Q_u	F_1	Q_u	F_1	Q_u	F_1	Q_u	F_1	Q_u	F_1	Q_u	F_1	Q_u	F_1	Q_u	F_1	Q_u
S_I	T_1	-		98.2	96.4	-		97.9	95.8	-		100	100	-		99.8	99.7	-		100	100
	T_2	34.0	20.5	58.4	41.2	79.8	66.4	85.8	75.1	53.8	36.8	79.3	65.7	96.0	92.4	96.3	92.8	**98.5**	**97.0**	**99.0**	**98.0**
	T_3	-		97.1	94.3	-		97.6	95.3	-		98.4	96.8	-		96.7	93.6	-		**100**	**100**
Average		34.0	20.5	84.6	77.3	79.8	66.4	93.8	88.7	53.8	36.8	92.6	87.5	96.0	92.4	97.6	95.4	**98.5**	**97.0**	**100**	**99.3**
S_{II}	T_1	40.9	25.7	54.3	37.3	41.2	25.9	66.6	49.9	49.0	32.5	78.1	64.0	87.9	78.4	95.1	90.7	**93.6**	**87.9**	**97.3**	**94.7**
	T_2	-		99.8	99.6	-		96.2	92.8	-		99.4	98.8	-		100	100	-		100	100
Average		40.9	25.7	77.1	68.6	41.2	25.9	81.4	71.4	49.0	32.5	88.8	81.4	87.9	78.4	97.6	95.4	**93.6**	**87.9**	**98.7**	**97.4**

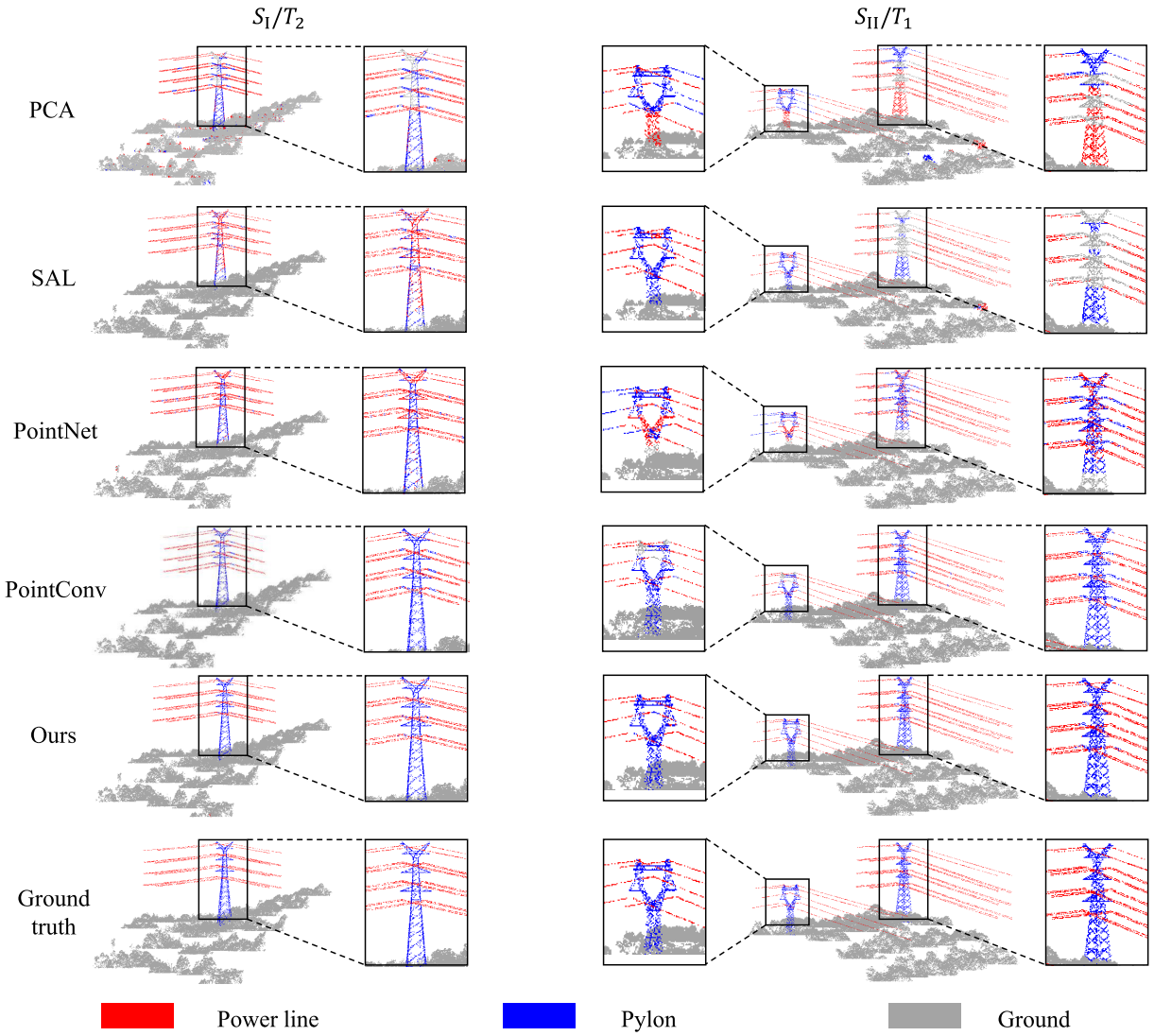

Fig. 8. Segmentation results. The power line, pylon, and ground (including vegetation) are colored in red, blue, and gray, respectively.

different modules. As shown in Table V, DGCNN has a good effect in the scene with only power lines, while the scene with pylons has a poor effect. Specifically, DGCNN achieves more than 99% in both F_1 and Q_u in the former case, while in the latter case, the power line is only 95.8% and 92%, and that of the pylon is only 94.3% and 89.3% in the dataset S_I. What is worse, in the dataset S_{II}, the F_1 and Q_u of the power line are only 93.8% and 88.3%, and that of the pylon is only 85.2% and 74.2%. From this phenomenon, it can be seen that for the DGCNN, the appearance of pylons seriously affects the segmentation result. Our proposed method achieves 100% in both F_1 and Q_u, and has a significant improvement compared to DGCNN.

NDI module is designed to enrich the input information and provide the network with local geometric features of the point clouds. Table V shows that after adding the NDI module, the segmentation results have improved significantly. For S_I/T_2, the F_1 and Q_u of the power line are increased by

TABLE IV
COMPUTATION TIME COMPARISONS AMONG DIFFERENT SEGMENTATION METHOD IN SECONDS (s)

Data set		PCA	SAL	PointNet	PointConv	Ours
S_I	T_1	170.16	204.48	0.45	2.58	2.76
	T_2	186.32	216.04	0.37	2.63	2.75
	T_3	185.56	197.04	0.37	2.73	2.74
Average		180.68	205.86	0.40	2.65	2.75
S_{II}	T_1	199.44	238.44	0.38	2.70	3.04
	T_2	183.64	209.76	0.38	2.71	2.71
Average		191.54	224.10	0.38	2.71	2.88

1.5% and 2.8%, and that of the pylon is increased by 2.3% and 4.1%. Meanwhile, for S_{II}/T_1, the results of power lines are improved by 1.2% and 2.1%, and that of the pylons are improved by 5.9% and 10.2%. This demonstrates that the local geometric features acquired by our NDI module can obtain a distinguished global feature.

As discussed in Section III, the local geometric features provided by the NDI module cannot be completely retained after MLP. Therefore, we designed the module to use the shallow local geometric features as input and aggregate the features through MLP and max-pooling operations. Table V presents the comparative results. It can be seen that after adding the NGIA modules, our method has been further improved compared to "DGCNN + NDI." Compared with DGCNN, in S_I/T_2, the F_1 and Q_u of the power line are raised by 2.7% and 5.1%, and that of the pylon is increased by 3.2% and 5.8%. Meanwhile, in S_{II}/T_1, the F_1 and Q_u of the power line are increased by 3.2% and 5.8%, and that of the pylon is improved by 7.4% and 5.8%, respectively. This proves the effectiveness of adding aggregated neighborhood geometric features to the final feature map through short branches.

AF module is proposed to aggregate the feature extracted from the up and down branches. It can be seen from Table V that compared with the DGCNN, in scenario S_I/T_2, our method exceeds 3.2% and 6% in F_1 and Q_u of the power line, and that of the pylon also improves 3.9% and 7.7%. Meanwhile, in scenario S_{II}/T_1, our method also obtains 3.5% and 6.4% improvement of F_1 and Q_u of the power line, and that of the pylon also improves 7.4% and 13.7%. This is attributed to the feature selector-like attention fusion module, which generates a soft attention mask to enhance useful features and discard unimportant features.

Besides, we evaluated the time consumption of each module. Table VI shows the RT of each module. It can be observed that NDI module is the most time-consuming because NDI needs to calculate the covariance matrix and solve the eigenvalues to obtain the dimension features. Besides, NGIA module takes only the result of the NDI module as input and computes the roughness features, which leads to the highest time efficiency. Compared with the basic method, our method only requires additional 0.5 s (0.48 s in S_I, and 0.49 s in S_{II}) but increases the F_1 and Q_u by 4.5% and 8.5%, respectively.

E. Power Line Identification and Reconstruction Results

To verify the effectiveness of power line identification, we compared it with existing methods. The metric is

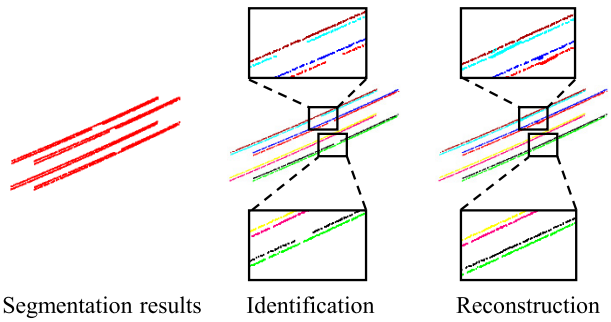

Fig. 9. Power line identification and reconstruction results. In the identification stage, all points of an individual power line are labeled with the same color.

identification rate, which is defined as

$$\text{Identification rate} = \frac{1}{n}\sum_{i=1}^{n}\frac{N_{\text{identified}_i}}{N_{\text{raw}_i}} \tag{11}$$

where n denotes the number of individual power lines in the scene. N_{raw_i} and $N_{\text{identified}_i}$ represent the number of the raw and identified ith individual power lines, respectively.

The alignment characteristics of the wires in the voxel grid [22] are used to extract single wire points, which is referred to as Baseline_1. HT and elevation threshold [24] is denoted as Baseline_2. Table VII shows the comparison results. It can be seen that compared to Baseline_1, the identification rate of our method is improved by 10%. In the dataset S_{II}, where there are two types of power lines, the identification rate of Baseline_1 is only about 85%, while our LSC method is above 99%. Meanwhile, our method is also 2% higher than the Baseline_2. The best performance of our method lies in the LSC. It can fit planes to ensure that the points of the same power line are identified, then the stable and complete identification results can be obtained. Moreover, the parameter setting of our method is simple. There is no need to set the number of power lines in advance. Line reconstruction is the final and important step. As shown in Fig. 9, several broken parts of power lines are well reconstructed.

F. Parameter Sensitivity Test

There are three important parameters in our GCN framework: the number of nearest points k in the segmentation phase and the distances d_{p_1} and d_{p_2} in the power line identification phase. To evaluate the influence of different settings on the performance of our method, we conducted several comparison experiments. Specifically, the optimization spaces for k, d_{p_1}, d_{p_2} were set as {10, 20, 30}, {0.11, 0.13, 0.15, 0.17, 0.19, 0.21, 0.23, 0.25, 0.27, 0.29} and {1, 2, 3, 4, 5, 6, 7, 8, 9, 10}, where the optimal parameter set is {20, 0.25 m, 5 m}.

1) Number of Nearest Neighbor Points k: We evaluate the performance of our method by varying k. Fig. 10(a) and (b) shows that when k increases from 10 to 20, the performance of our method improves significantly. This is because our method can encode more local information with a larger k. As k increases to 30, our method has a small improvement since more neighborhood points cannot provide more local

TABLE V

PERFORMANCE COMPARISONS AMONG DIFFERENT MODULES IN F_1 SCORE (%) AND QUALITY (%)

Data set		DGCNN				DGCNN+NDI				DGCNN+NDI+NGIA				DGCNN+NDI+NGIA+AF(Ours)			
		Pylon		Line		Pylon		Line		Pylon		Line		Pylon		Line	
		F_1	Q_u	F_1	Q_u	F_1	Q_u	F_1	Q_u	F_1	Q_u	F_1	Q_u	F_1	Q_u	F_1	Q_u
S_I	T_1	-		100	100	-		100	100	-		100	100	-		100	100
	T_2	94.3	89.3	95.8	92.0	96.6	93.4	97.3	94.8	97.5	95.1	98.5	97.1	**98.5**	**97.0**	**99.0**	**98.0**
	T_3	-		99.8	99.6	-		99.8	99.5	-		99.9	99.8	-		**100**	**100**
Average		94.3	89.3	98.5	97.2	96.6	93.4	99.0	98.1	97.5	95.1	99.5	99.0	**98.5**	**97.0**	**99.7**	**99.3**
S_{II}	T_1	85.2	74.2	93.8	88.3	91.6	84.6	96.2	92.6	92.6	86.2	97.0	94.1	**93.6**	**87.9**	**97.3**	**94.7**
	T_2	-		100	100	-		100	100	-		99.7	99.5	-		100	100
Average		85.2	74.2	96.9	94.2	91.6	84.6	98.1	96.3	92.6	86.2	98.4	97.0	**93.6**	**87.9**	**98.7**	**97.4**

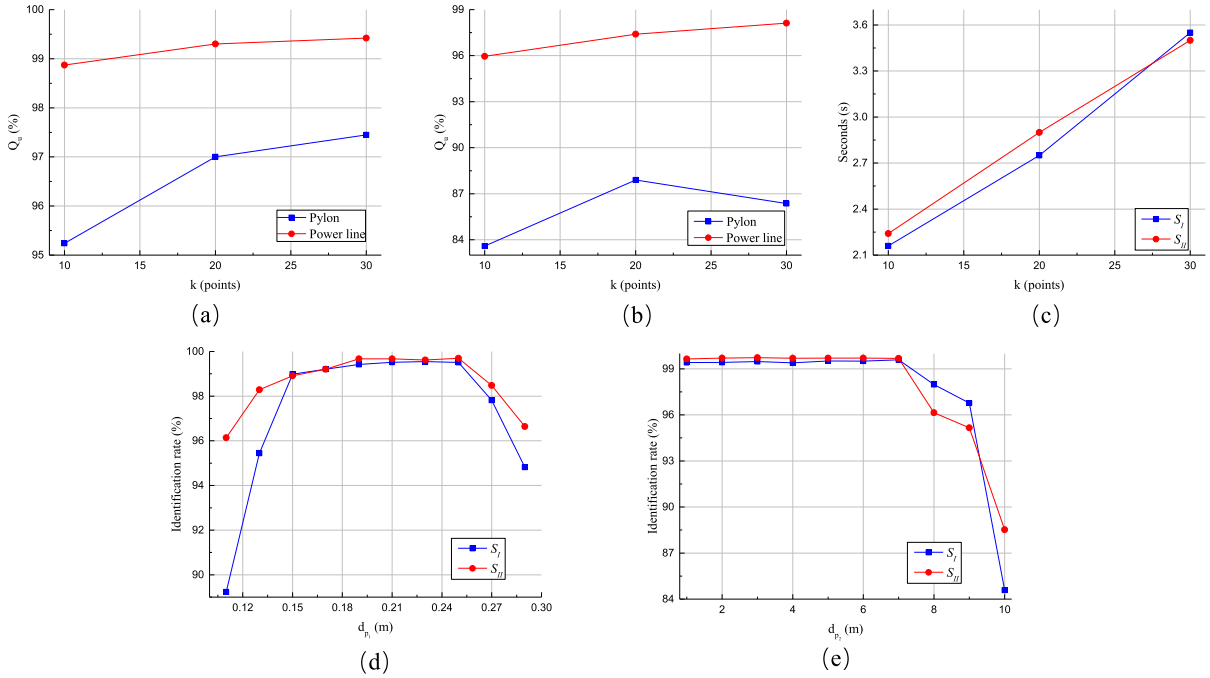

Fig. 10. Performance of different parameters. (a) and (b) Performance of k (number of points) in S_I and S_{II}, respectively. (c) Time comparison of different k in both two scenes. (d) and (e) Performance of d_{p_1} and d_{p_2} in both two scenes, respectively.

TABLE VI

COMPUTATION TIME COMPARISONS AMONG DIFFERENT MODULES IN SECONDS (s)

Data set		DGCNN	NDI	NGIA	AF	Ours
S_I	T_1	2.35	0.19	0.09	0.16	2.79
	T_2	2.24	0.27	0.08	0.16	2.75
	T_3	2.24	0.26	0.10	0.14	2.74
Average		2.28	0.24	0.09	0.16	2.76
S_{II}	T_1	2.45	0.30	0.09	0.20	3.04
	T_2	2.25	0.28	0.08	0.14	2.71
Average		2.35	0.29	0.09	0.17	2.88

TABLE VII

PERFORMANCE COMPARISONS AMONG DIFFERENT IDENTIFICATION METHOD IN IDENTIFICATION RATE (%)

Data set		Number of lines	Baseline_1	Baseline_2	Ours
S_I	T_1	14	93.17	99.32	**99.80**
	T_2	14	90.24	98.85	**98.95**
	T_3	14	82.23	99.16	**99.78**
Average			88.55	99.11	**99.51**
S_{II}	T_1	19	84.52	99.36	**99.63**
	T_2	19	84.80	91.48	**99.77**
Average			84.66	95.42	**99.70**

information for our model. As shown in Fig. 10(c), the time consumption with $k = 30$ is significantly larger than that with $k = 20$. To balance the performance and time consumption, we set $k = 20$.

2) Point-to-Plane Distance Threshold d_{p_1} and d_{p_2}: d_{p_1} and d_{p_2} represent the distance thresholds from the point to the fitting plane p_1 and vertical plane p_2, respectively, which are used to make the identified points be classified as the same power line. We used the grid search strategy to find the optimal combination. We evaluated different values of d_{p_1} on two test datasets while keeping $d_{p_2} = 5$ m. As shown in Fig. 10(d), when d_{p_1} goes from 0.11 to 0.19 m, the identification rate increases, and the recall rate increases as the increase of d_{p_1}. It is also observed that d_{p_1} within the range of [0.19 m, 0.25 m] could produce stable results. That is, most of the points have been correctly identified for the ith individual power line. As d_{p_1} increases, the identification rate decreases sharply

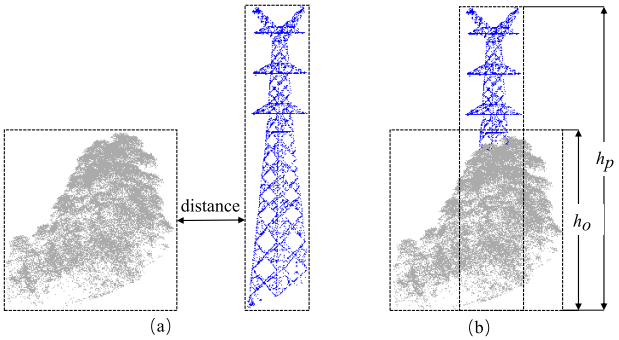

Fig. 11. Generated two kinds of complex scenes. (a) Trees exist around the pylon. (b) Trees occlude the pylon.

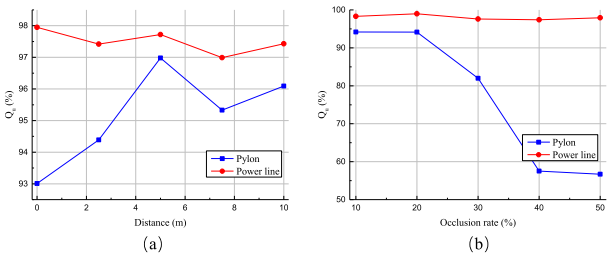

Fig. 12. Performance comparisons with different (a) distance and (b) occlusion rate in quality.

because the ith power line points are incorrectly identified as the jth power line. Similarly, we evaluated different values of d_{p_2} on two test datasets while keeping $d_{p_1} = 0.25$ m. Fig. 10(e) shows d_{p_2} within the range of [1 m, 7 m] can produce promising results. Therefore, we set $d_{p_1} = 0.25$ m and $d_{p_2} = 5$ m to provide excellent performance.

G. Robustness Test

In this section, we evaluated the robustness for the semantic segmentation stage and line identification stage, respectively. To evaluate our semantic segmentation method in the occlusion case, we used scene S_1/T_2 to generate complex scenes to test the performance of our method. To test the robustness of our segmentation method, we conducted experiments for two cases. For case 1, as shown in Fig. 11(a), we changed the distance between the tree and pylon and evaluated the performance of our method. For case 2, as shown in Fig. 11(b), we tested the performance of our method with a given occlusion rate, which is defined as follows:

$$\text{Occlusion rate} = \frac{\text{volume of occlusion space}}{\text{volume of pylon space}} = \frac{h_o}{h_p} \quad (12)$$

where h_o/h_p is the height of occlusion/pylon space.

Fig. 12(a) shows the influence of distance on the performance of our method. It can be seen that when the distance = 0, the Q_u of the extracted pylon is still above 93%. For the distance within the range of [0, 5 m], the Q_u of the extracted pylon increases as the distance increases and remains stable after the distance above 5 m. Fig. 12(b) shows the results of our method with different occlusion rates. When the occlusion rate is less than 0.3, our method can extract the pylon completely. Even in the situation of occlusion rate = 0.5, Q_u of the pylon is above 56%. The result of the second case is worse because the pylon in the first case remains a relatively complete structure, which can provide more useful information. In addition, Q_u of the power line is always above 97% in both cases. This experiment proves that our semantic segmentation method is robust to occlusion.

Most of the current methods can only be applied to a single scene. To verify our power line identification method in different cases, we used two types of power lines to generate complex scenes to test the performance of our method, including disconnection in the middle (case 1), disconnection on both sides (case 2), cross (case 3) and compound cases (case 4). To better describe the complex scene we generated, the cross-angle is defined as the angle between the two types of power line horizontal plane projections, and the disconnection rate defined as

$$\text{Disconnection rate} = \frac{\text{disconnection length}}{\text{total length}}. \quad (13)$$

We generate scenes with a disconnection rate of 10% and 20% for both cases 1 and 2, and case 3 with a cross-angle of 10° and 20°. Case 4 is a scene with all disturbance.

Fig. 13 shows the identification results of our method in four cases. In this stage, all points of an individual power line are labeled with the same color. Table VIII shows the identification rate of our method, which has achieved satisfactory results, larger than 98% in various scenarios. These experiments prove that our LSC method is robust and can be applied to various complex scenarios.

IV. Discussion

Experiments show that the proposed method outperforms other existing methods. Moreover, the proposed method only uses the unstructured ALS point cloud in the XYZ format, which makes the proposed method more widely used. The superior results of our method can be attributed to the following reasons.

1) In the preprocessing stage, the proposed data augmentation method generates a sufficient amount of diverse training samples. Besides, the designed near-ground filtering method can remove ground points as much as possible while preserving the power line and pylon points.
2) In the power line and pylon segmentation stage, we propose a new method based on GCN, which mainly includes two modules, NDI and NGIA. These two modules are designed to provide local geometry and detailed features of objects. Finally, the AF module is used to fuse multichannel features to obtain shallow geometric features effectively and high-level semantic features.
3) In the power line identification stage, our LSC method robustly identifies all points of an individual power line and reconstruct the broken power lines simultaneously by fitting a polynomial.

Future Work: As shown in Fig. 8, our method also has incomplete extraction results of pylon and power line points

TABLE VIII

IDENTIFICATION RATE (%) IN DIFFERENT COMPLEX SCENARIOS. NOTE THAT THE PERCENTAGE (%) AND ANGLE (°) IN THE SECOND ROW OF TABLE REPRESENT DISCONNECTION RATE AND CROSS-ANGLE, RESPECTIVELY

Power	Case 1		Case 2		Case 3		Case 4	
line type	10%	20%	10%	20%	10°	20°	10°	20°
I	99.7	99.7	99.8	99.7	99.4	99.0	99.0	98.9
II	99.3	99.0	99.8	99.6				

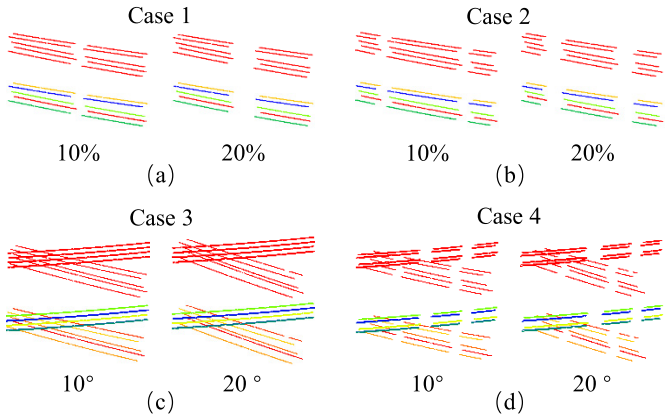

Fig. 13. Results of four disturbance cases. (a) Disconnection in the middle with different percentages. (b) Disconnection on both sides with different percentages. (c) Cross with different angles. (d) Compound cases with all disturbances. The percentage and angle refer to interruption rate and cross-angle respectively and all points of an individual power line are labeled with the same color.

in some extremely complex scenes, especially at the junction of two types of objects. In future work, we will combine multisource data such as images to improve the extraction results.

V. CONCLUSION

This article presented a new method based on GCN to efficiently and accurately extract pylon and power line points from ALS data. First, for the power line scenes, an effective data augmentation algorithm and near-ground filtering algorithm were proposed to solve the problem of insufficient data and sample imbalance. Second, based on the GCN network, a dual-branch network method was designed. The up branch uses the NDI module to enrich the input information and obtains rich low-level geometric and high-level semantic information by multiple EdgeConvs and MLP. The down branch uses the NGIA module to enhance the description ability of the pylon and power line. We used the attention mechanism to strengthen the feature aggregation effect of the up and down branches. Finally, an LSC algorithm was proposed to identify power lines, and we used the least-squares method to fit polynomials to reconstruct power lines. Our experiments proved that our extraction method could effectively extract pylon and power line points. The F_1 score and quality of the power line reach 99.3% and 98.6%, and the results of the pylon reach 96% and 92.4%, respectively. The identification rate of our power line identification method is above 98%.

REFERENCES

[1] S. J. Mills *et al.*, "Evaluation of aerial remote sensing techniques for vegetation management in power-line corridors," *IEEE Trans. Geosci. Remote Sens.*, vol. 48, no. 9, pp. 3379–3390, Sep. 2010.

[2] Y. Pradeep, S. A. Khaparde, and R. K. Joshi, "High level event ontology for multiarea power system," *IEEE Trans. Smart Grid*, vol. 3, no. 1, pp. 193–202, Mar. 2012.

[3] Z. Li, T. S. Bruggemann, J. J. Ford, L. Mejias, and Y. Liu, "Toward automated power line corridor monitoring using advanced aircraft control and multisource feature fusion," *J. Field Robot.*, vol. 29, no. 1, pp. 4–24, Jan. 2012.

[4] M. Shahzad, M. Maurer, F. Fraundorfer, Y. Wang, and X. X. Zhu, "Buildings detection in VHR SAR images using fully convolution neural networks," *IEEE Trans. Geosci. Remote Sens.*, vol. 57, no. 2, pp. 1100–1116, Feb. 2019.

[5] L. Matikainen *et al.*, "Remote sensing methods for power line corridor surveys," *ISPRS J. Photogramm. Remote Sens.*, vol. 119, pp. 10–31, Sep. 2016.

[6] Z. Zhang, L. Zhang, Y. Tan, L. Zhang, F. Liu, and R. Zhong, "Joint discriminative dictionary and classifier learning for ALS point cloud classification," *IEEE Trans. Geosci. Remote Sens.*, vol. 56, no. 1, pp. 524–538, Jan. 2018.

[7] B. Xiang, J. Tu, J. Yao, and L. Li, "A novel octree-based 3-D fully convolutional neural network for point cloud classification in road environment," *IEEE Trans. Geosci. Remote Sens.*, vol. 57, no. 10, pp. 7799–7818, Oct. 2019.

[8] V. N. Nguyen, R. Jenssen, and D. Roverso, "Automatic autonomous vision-based power line inspection: A review of current status and the potential role of deep learning," *Int. J. Electr. Power Energy Syst.*, vol. 99, pp. 107–120, Jul. 2018.

[9] J. Jung, E. Che, M. J. Olsen, and K. C. Shafer, "Automated and efficient powerline extraction from laser scanning data using a voxel-based subsampling with hierarchical approach," *ISPRS J. Photogramm. Remote Sens.*, vol. 163, pp. 343–361, May 2020.

[10] P. Axelsson, "DEM generation from laser scanner data using adaptive TIN models," in *Proc. Ann. Photogramm. Remote Sens. Spat. Inf. Sci. (ISPRS)*, vol. 33, 2000, pp. 85–92.

[11] W. Zhang *et al.*, "An easy-to-use airborne LiDAR data filtering method based on cloth simulation," *Remote Sens.*, vol. 8, no. 6, pp. 501–522, 2016.

[12] L. Cheng, L. Tong, Y. Wang, and M. Li, "Extraction of urban power lines from vehicle-borne LiDAR data," *Remote Sens.*, vol. 6, no. 4, pp. 3302–3320, Apr. 2014.

[13] X. Shen, C. Qin, Y. Du, X. Yu, and R. Zhang, "An automatic extraction algorithm of high voltage transmission lines from airborne LIDAR point cloud data," *Turkish J. Electr. Eng. Comput. Sci.*, vol. 26, no. 4, pp. 2043–2055, Jul. 2018.

[14] M. Lehtomäki, A. Kukko, L. Matikainen, J. Hyyppä, H. Kaartinen, and A. Jaakkola, "Power line mapping technique using all-terrain mobile laser scanning," *Autom. Constr.*, vol. 105, pp. 1–16, Sep. 2019.

[15] S. Xu and R. Wang, "Power line extraction from mobile LiDAR point clouds," *IEEE J. Sel. Topics Appl. Earth Observ. Remote Sens.*, vol. 12, no. 2, pp. 734–743, Feb. 2019.

[16] H. B. Kim and G. Sohn, "Point-based classification of power line corridor scene using random forests," *Photogramm. Eng. Remote Sens.*, vol. 79, no. 9, pp. 821–833, Sep. 2013.

[17] B. Guo, X. Huang, F. Zhang, and G. Sohn, "Classification of airborne laser scanning data using JointBoost," *ISPRS J. Photogramm. Remote Sens.*, vol. 100, pp. 71–83, Feb. 2015.

[18] Y. Wang, Q. Chen, L. Liu, D. Zheng, C. Li, and K. Li, "Supervised classification of power lines from airborne LiDAR data in urban areas," *Remote Sens.*, vol. 9, no. 8, pp. 771–787, 2017.

[19] Y. Wang, Q. Chen, L. Liu, X. Li, A. Sangaiah, and K. Li, "Systematic comparison of power line classification methods from ALS and MLS point cloud data," *Remote Sens.*, vol. 10, no. 8, pp. 1222–1240, 2018.

[20] B. Guo, Q. Li, X. Huang, and C. Wang, "An improved method for power-line reconstruction from point cloud data," *Remote Sens.*, vol. 8, no. 36, pp. 17–34, 2016.

[21] J. Yang and Z. Kang, "Voxel-based extraction of transmission lines from airborne LiDAR point cloud data," *IEEE J. Sel. Topics Appl. Earth Observ. Remote Sens.*, vol. 11, no. 10, pp. 3892–3904, Oct. 2018.

[22] N. Munir, M. Awrangjeb, B. Stantic, G. Lu, and S. Islam, "Voxel-based extraction of individual pylons and wires from LiDAR point cloud data," *ISPRS Ann. Photogramm., Remote Sens. Spatial Inf. Sci.*, vol. IV-4/W8, pp. 91–98, Sep. 2019.

[23] Y. Jwa, G. Sohn, and H. Kim, "Automatic 3D powerline reconstruction using airborne LiDAR data," in *Proc. Ann. Photogramm. Remote Sens. Spat. Inf. Sci. (ISPRS)*, vol. 38, 2009, pp. 105–110.

[24] M. Yadav and C. G. Chousalkar, "Extraction of power lines using mobile LiDAR data of roadway environment," *Remote Sens. Appl., Soc. Environ.*, vol. 8, pp. 258–265, Nov. 2017.

[25] Y. LeCun, Y. Bengio, and G. Hinton, "Deep learning," *Nature*, vol. 521, no. 7553, pp. 436–444, May 2015.

[26] X. Lu *et al.*, "Multi-scale and multi-task deep learning framework for automatic road extraction," *IEEE Trans. Geosci. Remote Sens.*, vol. 57, no. 11, pp. 9362–9377, Nov. 2019.

[27] J. Geng, H. Wang, J. Fan, and X. Ma, "SAR image classification via deep recurrent encoding neural networks," *IEEE Trans. Geosci. Remote Sens.*, vol. 56, no. 4, pp. 2255–2269, Apr. 2018.

[28] L. Mou and X. X. Zhu, "Vehicle instance segmentation from aerial image and video using a multitask learning residual fully convolutional network," *IEEE Trans. Geosci. Remote Sens.*, vol. 56, no. 11, pp. 6699–6711, Nov. 2018.

[29] H. Su, S. Maji, E. Kalogerakis, and E. Learned-Miller, "Multi-view convolutional neural networks for 3D shape recognition," in *Proc. IEEE Int. Conf. Comput. Vis. (ICCV)*, Dec. 2015, pp. 945–953.

[30] Z. Luo, J. Li, Z. Xiao, Z. G. Mou, X. Cai, and C. Wang, "Learning high-level features by fusing multi-view representation of MLS point clouds for 3D object recognition in road environments," *ISPRS J. Photogramm. Remote Sens.*, vol. 150, pp. 44–58, Apr. 2019.

[31] G. Riegler, A. O. Ulusoy, and A. Geiger, "OctNet: Learning deep 3D representations at high resolutions," in *Proc. IEEE Conf. Comput. Vis. Pattern Recognit. (CVPR)*, Jul. 2017, pp. 6620–6629.

[32] Y. Zhou and O. Tuzel, "VoxelNet: End-to-end learning for point cloud based 3D object detection," in *Proc. IEEE/CVF Conf. Comput. Vis. Pattern Recognit. (CVPR)*, Jun. 2018, pp. 4490–4499.

[33] R. Q. Charles, H. Su, M. Kaichun, and L. J. Guibas, "PointNet: Deep learning on point sets for 3D classification and segmentation," in *Proc. IEEE Conf. Comput. Vis. Pattern Recognit. (CVPR)*, Jul. 2017, pp. 77–85.

[34] Z. Luo *et al.*, "Learning sequential slice representation with an attention-embedding network for 3D shape recognition and retrieval in MLS point clouds," *ISPRS J. Photogramm. Remote Sens.*, vol. 161, pp. 147–163, Mar. 2020.

[35] Y. Wang, Y. Sun, and Z. Liu, "Dynamic graph CNN for learning on point cloud," *ACM Trans. Graph.*, vol. 38, no. 5, pp. 1–12, 2019.

[36] Y. Guo, H. Wang, Q. Hu, H. Liu, L. Liu, and M. Bennamoun, "Deep learning for 3D point clouds: A survey," *IEEE Trans. Pattern Anal. Mach. Intell.*, early access, Jun. 29, 2020, doi: 10.1109/TPAMI.2020.3005434.

[37] C. Qi, Y. Li, H. Su, and L. Guibas, "PointNet++: Deep hierarchical feature learning on point sets in a metric space," in *Proc. Neural Inf. Process. Syst. (NeurIPS)*, 2017, pp. 1–10.

[38] W. Wu, Z. Qi, and L. Fuxin, "PointConv: Deep convolutional networks on 3D point clouds," in *Proc. IEEE/CVF Conf. Comput. Vis. Pattern Recognit. (CVPR)*, Jun. 2019, pp. 9621–9630.

[39] I. Armeni *et al.*, "3D semantic parsing of large-scale indoor spaces," in *Proc. IEEE Conf. Comput. Vis. Pattern Recognit. (CVPR)*, Jun. 2016, pp. 1534–1543.

[40] A. Dai, A. X. Chang, M. Savva, M. Halber, T. Funkhouser, and M. Niessner, "ScanNet: Richly-annotated 3D reconstructions of indoor scenes," in *Proc. IEEE Conf. Comput. Vis. Pattern Recognit. (CVPR)*, Jul. 2017, pp. 2432–2443.

[41] T. Hackel, N. Savinov, L. Ladicky, J. Wegner, K. Schindler, and M. Pollefeys, "Semantic3D.net: A new large-scale point cloud classification benchmark," in *Proc. Ann. Photogramm. Remote Sens. Spat. Inf. Sci. (ISPRS)*, vol. IV-1/W1, 2017, pp. 91–98.

[42] J. Behley *et al.*, "SemanticKITTI: A dataset for semantic scene understanding of LiDAR sequences," in *Proc. IEEE/CVF Int. Conf. Comput. Vis. (ICCV)*, Oct. 2019, pp. 2432–2443.

[43] L. Zhu and J. Hyyppä, "Fully-automated power line extraction from airborne laser scanning point clouds in forest areas," *Remote Sens.*, vol. 6, no. 11, pp. 11267–11282, Nov. 2014.

[44] H. Hanraz, N. Jacobs, M. Contreras, and C. Clark, "Deep learning for conifer/deciduous classification of airborne LiDAR 3D point clouds representing individual trees," *ISPRS-J. Photogramm. Remote Sens.*, vol. 158, pp. 230–2019, Dec. 2019.

[45] J.-F. Lalonde, N. Vandapel, D. F. Huber, and M. Hebert, "Natural terrain classification using three-dimensional ladar data for ground robot mobility," *J. Field Robot.*, vol. 23, no. 10, pp. 839–861, Oct. 2006.

[46] K. He, X. Zhang, S. Ren, and J. Sun, "Deep residual learning for image recognition," in *Proc. IEEE Conf. Comput. Vis. Pattern Recognit. (CVPR)*, Jun. 2016, pp. 770–778.

[47] F. Wang *et al.*, "Residual attention network for image classification," in *Proc. IEEE Conf. Comput. Vis. Pattern Recognit. (CVPR)*, Jul. 2017, pp. 6450–6458.

[48] D. Yoo, S. Park, J.-Y. Lee, A. S. Paek, and I. S. Kweon, "AttentionNet: Aggregating weak directions for accurate object detection," in *Proc. IEEE Int. Conf. Comput. Vis. (ICCV)*, Dec. 2015, pp. 2659–2667.

[49] J. Hu, L. Shen, S. Albanie, G. Sun, and E. Wu, "Squeeze-and-excitation networks," *IEEE Trans. Pattern Anal. Mach. Intell.*, vol. 42, no. 8, pp. 2011–2023, Aug. 2020.

[50] H. Beaty, H. Beaty, and D. Fink, "Standard handbook for electrical engineers sixteenth edition," *Nature*, vol. 15, no. 111, pp. 458–459, 2013.

Wen Li (Student Member, IEEE) received the B.Eng. degree in communication engineering from the School of Information Science and Technology, Shandong Agricultural University, Taian, China, in 2018. He is pursuing the M.Eng. degree in electronic and communication engineering with the Fujian Key Laboratory of Sensing and Computing for Smart Cities, School of Informatics, Xiamen University, Xiamen, China.

His research interests include LiDAR data processing, 3-D computer vision, and machine learning.

Zhipeng Luo (Student Member, IEEE) received the Ph.D. degree in information and communications engineering from Xiamen University, Xiamen, China, in 2020.

He is currently a Research Assistant Professor with the Department of Land Surveying and Geo-Informatics, The Hong Kong Polytechnic University, Hong Kong. He has published articles in the *ISPRS Journal of Photogrammetry and Remote Sensing*, the IEEE TRANSACTIONS ON INTELLIGENT TRANSPORTATION SYSTEMS, and the IEEE JOURNAL OF SELECTED TOPICS IN APPLIED EARTH OBSERVATIONS AND REMOTE SENSING. His research interests include autonomous driving, mobile laser scanning, intelligent processing of point clouds, 3-D computer vision, and machine learning.

Zhenlong Xiao (Member, IEEE) received the B.S. degree from the Nanjing University of Posts and Telecommunications, Nanjing, China, in 2008, the M.S. degree from the Beijing University of Posts and Telecommunications, Beijing, China, in 2011, and the Ph.D. degree from The Hong Kong Polytechnic University, Hong Kong, in 2015.

He is an Associate Professor with the Department of Informatics and Communication Engineering, School of Informatics, Xiamen University, Xiamen, China. His research interests include the nonlinear signal processing, graph signal processing, collaborative signal processing, and structural health monitoring.

Yiping Chen (Senior Member, IEEE) received the Ph.D. degree in information and communications engineering from the National University of Defense Technology, Changsha, China, in 2011.

She is a Senior Engineer with the Fujian Key Laboratory of Sensing and Computing for Smart Cities, School of Informatics, Xiamen University, Xiamen, China. From 2007 to 2011, she was an Assistant Researcher with The Chinese University of Hong Kong, Hong Kong. Her research interests include image processing, mobile laser scanning data analysis, 3-D point cloud computer vision, and autonomous driving.

Cheng Wang (Senior Member, IEEE) received the Ph.D. degree in signal and information processing from the National University of Defense Technology, Changsha, China, in 2002.

He is a Professor with the School of Informatics, and the Executive Director with the Fujian Key Laboratory of Sensing and Computing for Smart Cities, Xiamen University, Xiamen, China. He has coauthored more than 150 articles in referred journals and top conferences, including the IEEE TRANSACTIONS ON GEOSCIENCE AND REMOTE SENSING, *Pattern Recognition* , the IEEE TRANSACTIONS ON INTELLIGENT TRANSPORTATION SYSTEMS, the IEEE Conference on Computer Vision and Pattern Recognition, the Association for the Advancement of Artificial Intelligence (AAAI), and the International Society for Photogrammetry and Remote Sensing (ISPRS) *Journal of Photogrammetry and Remote Sensing*. His research interests include point cloud analysis, multisensory fusion, mobile mapping, and geospatial big data.

Dr. Wang is a fellow of the Institution of Engineering and Technology and an Associate Editor of the IEEE GEOSCIENCE AND REMOTE SENSING LETTERS. He is also the Chair of the Working Group I/6 on Multi-Sensor Integration and Fusion of the ISPRS.

Jonathan Li (Senior Member, IEEE) received the Ph.D. degree in geomatics engineering from the University of Cape Town, Cape Town, South Africa, in 2000.

He is a Professor with both the Department of Geography and Environmental Management and the Department of Systems Design Engineering, University of Waterloo, Waterloo, ON, Canada. He has coauthored more than 400 publications, including over 270 refereed journal papers. His main research interests include image and point cloud analytics, mobile mapping, and AI-powered information extraction from LiDAR point clouds and earth observation images.

Dr. Li was a recipient of the Outstanding Achievement in Mobile Mapping Technology Award in 2019 for his pioneering contributions in developing and promoting mobile mapping technology and the ISPRS Samuel Gamble Award in 2020 for his significant contributions to the development, organization, or professional activities of the photogrammetry, remote sensing, and spatial information sciences at national or international level. He is currently serving as the Associate Editor of IEEE TRANSACTIONS ON INTELLIGENT TRANSPORTATION SYSTEMS, IEEE TRANSACTIONS ON GEOSCIENCE AND REMOTE SENSING, and *Canadian Journal of Remote Sensing*. He has been the Editor-in-Chief of the International Journal of Applied Earth Observation and Geoinformation since January 2021.